




Article

Macrophage-Laden Gold Nanoflowers Embedded with Ultrasmall Iron Oxide Nanoparticles for Enhanced Dual-Mode CT/MR Imaging of Tumors

Yucheng Peng ^{1,†}, Xiaomeng Wang ^{1,†}, Yue Wang ², Yue Gao ¹, Rui Guo ¹ , Xiangyang Shi ^{1,*}  and Xueyan Cao ^{1,*} 

- ¹ Shanghai Engineering Research Center of Nano-Biomaterials and Regenerative Medicine, College of Chemistry, Chemical Engineering and Biotechnology, Donghua University, Shanghai 201620, China; wang320333@gmail.com (Y.P.); 04200005@sues.edu.cn (X.W.); gaoyue@mail.dhu.edu.cn (Y.G.); ruiguo@dhu.edu.cn (R.G.)
- ² Department of Radiology, Shanghai Songjiang District Central Hospital, Shanghai 201600, China; lzyang0816@gmail.com
- * Correspondence: xshi@dhu.edu.cn (X.S.); caoxy_116@dhu.edu.cn (X.C.)
- † The authors contributed equally to this work.



Citation: Peng, Y.; Wang, X.; Wang, Y.; Gao, Y.; Guo, R.; Shi, X.; Cao, X. Macrophage-Laden Gold Nanoflowers Embedded with Ultrasmall Iron Oxide Nanoparticles for Enhanced Dual-Mode CT/MR Imaging of Tumors. *Pharmaceutics* **2021**, *13*, 995. <https://doi.org/10.3390/pharmaceutics13070995>

Academic Editors: Emanuela Fabiola Craparo, Donatella Paolino and Twan Lammers

Received: 30 April 2021
Accepted: 25 June 2021
Published: 30 June 2021

Publisher's Note: MDPI stays neutral with regard to jurisdictional claims in published maps and institutional affiliations.



Copyright: © 2021 by the authors. Licensee MDPI, Basel, Switzerland. This article is an open access article distributed under the terms and conditions of the Creative Commons Attribution (CC BY) license (<https://creativecommons.org/licenses/by/4.0/>).

Abstract: The design of multimodal imaging nanoplatforms with improved tumor accumulation represents a major trend in the current development of precision nanomedicine. To this end, we report herein the preparation of macrophage (MA)-laden gold nanoflowers (NFs) embedded with ultrasmall iron oxide nanoparticles (USIO NPs) for enhanced dual-mode computed tomography (CT) and magnetic resonance (MR) imaging of tumors. In this work, generation 5 poly(amidoamine) (G5 PAMAM) dendrimer-stabilized gold (Au) NPs were conjugated with sodium citrate-stabilized USIO NPs to form hybrid seed particles for the subsequent growth of Au nanoflowers (NFs). Afterwards, the remaining terminal amines of dendrimers were acetylated to form the dendrimer-stabilized Fe₃O₄/Au NFs (for short, Fe₃O₄/Au DSNFs). The acquired Fe₃O₄/Au DSNFs possess an average size around 90 nm, display a high r₁ relaxivity (1.22 mM⁻¹ s⁻¹), and exhibit good colloidal stability and cytocompatibility. The created hybrid DSNFs can be loaded within MAs without producing any toxicity to the cells. Through the mediation of MAs with a tumor homing and immune evasion property, the Fe₃O₄/Au DSNFs can be delivered to tumors more efficiently than those without MAs after intravenous injection, thus significantly improving the MR/CT imaging performance of tumors. The developed MA-mediated delivery system may hold great promise for enhanced tumor delivery of other contrast agents or nanomedicines for precision cancer nanomedicine applications.

Keywords: gold nanoflowers; ultrasmall iron oxide nanoparticles; multimode imaging; macrophage; tumor diagnosis

1. Introduction

Molecular imaging techniques, based on various functional nanoparticles, have attracted increasing attention in the recent development of cancer nanomedicine which is critical for early tumor therapy guidance [1]. Among them, the development of nanoplatforms integrated with different imaging techniques such as computed tomography (CT)[2], ultrasound (US) [3], photoacoustic (PA) [4], and magnetic resonance (MR) [5] imaging represent a competitive strategy for precision cancer diagnoses. Iron oxide NPs have been adopted as negative contrast agents for MR technology due to the T₂-weighted effect [6]. Au NPs have been broadly used in CT technology and PTT (photothermal therapy) attributing to their intrinsic advantages of an excellent X-ray attenuation feature as well as a near-infrared (NIR) absorption property, respectively [7].

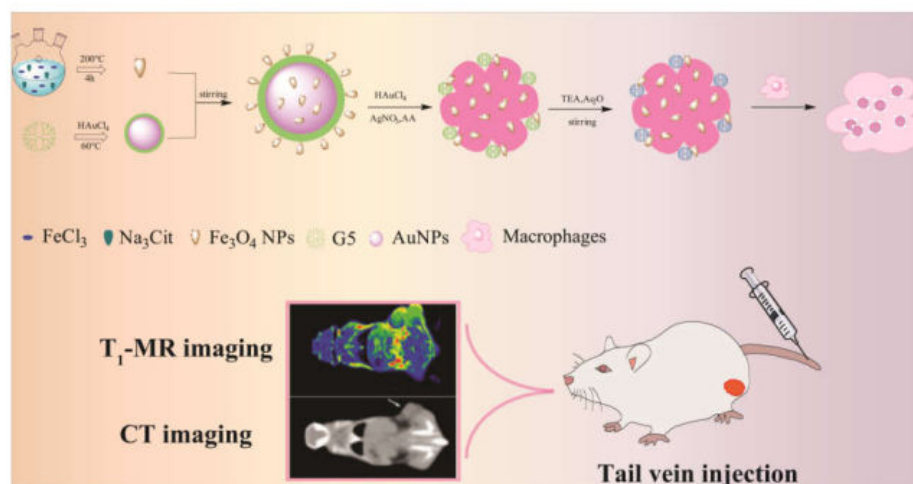
In order to realize the precision molecular imaging, it was desirable to incorporate both Fe₃O₄ NPs and Au NPs in one nanoplatform to achieve dual-modal MR/CT imaging [8].

However, to avoid the inaccurate results caused by negative contrast MR images which were hard to be discerned from the tumor site due to dark signal, alternative methods have been explored. Ultrasmall iron oxide (USIO) NPs with a dimension <5 nm have been confirmed and utilized as a promising T_1 -positive contrast agent [9]. Furthermore, the surface modification of USIO with functional moieties could further endow the NPs with targeting or antifouling properties. USIO NPs have also been applied as crosslinkers for alginate nanogels to enhance their r_1 relaxivity [10]. In addition, different shapes of Au NPs such as Au nanostars (NSs) [11], Au nanorods (NRs) [12], and Au NFs [13] have been confirmed to have good biosafety and high photothermal conversion efficiency [14], employed as a wonderful theranostic reagent for PA technology and PTT. In our previous studies, we have demonstrated that USIO NPs can be embedded within Au NFs to form Fe_3O_4/Au NFs with a high r_1 relaxivity, leading to the feasibility of multimodal MR/CT/PA imaging and combination PTT/radiotherapy (RT) of tumors [15]. However, considering the fact that NPs are easily non-specifically adsorbed by proteins in the blood vessels, and could be removed rapidly by the reticuloendothelial system (RES) [16], construction of a dual-modal imaging nanoplatfrom which possesses improved tumor penetration and accumulation abilities is still important and urgent.

To increase the payload at the tumor site, two major strategies are applied, which stand as passive targeting and active targeting. For passive targeting, NPs are directed to the enhanced permeability and retention (EPR) taking advantage of the leaky blood vessels of tumors. However, this targeting ability is mainly affected by the biophysicochemical characteristics of NPs [17], and can be largely weakened due to hypoxia and necrosis of central parts of tumors. While for active targeting, various kinds of targeting ligands are modified to recognize and bind to certain receptors specially expressed on tumor cells [18]. However, the previous study has demonstrated that the peak tumor uptake of the NPs with targeting ligand was $<2\%$ of the entire dosage [19]. Moreover, one targeting ligand is often limited to identify several certain types of tumors, thus lacking general applicability [20]. It is also noteworthy that the synthesis of the NPs with targeting ligands usually involve unfavorable complex preparation steps and expensive raw materials [21]. In addition, to overcome RES, a “stealth” strategy of NPs has recently been adopted. This strategy has been proven to have the advantage of avoiding clearance by macrophages; however, at the same time, it owns the disadvantage of suppressing the NPs’ internalization by target cells [22].

Toward these issues, tumor-directed cell-mediated drug delivery systems have become a major focus in cancer theranostics [23]. Specific cells are able to be used as vehicles to convey NPs across the cancer or along the cancer fringe to improve the accumulation of NPs. For instance, red blood cells [24], mesenchymal stem cells (MSCs) [25], neural stem cells [26], and macrophages (MAs) [27] have been regarded as effective tumor-targeting carriers. In addition, these cell-mediated delivery systems play to their inherent characteristics’ strengths, such as having the advantages of non-tumorigenic, low immunogenicity, and being able to cross certain physiological barriers in the body [28]. The FDA has approved a stem cells carrier to be used in clinical trials for glioma treatment. Among these cell vehicles [29], macrophages possess the unique advantages of minimized phagocytosis and extraction from peripheral blood, which is particularly critical in drug delivery. Previously, we have confirmed that MSCs-mediated delivery systems of nanogels with Fe_3O_4 NPs improved the magnetic MR effect in breast and glioma tumor models in comparison with free nanogels loaded with Fe_3O_4 NPs [30]. Recently, Guo et al. [31] treated ovarian cancer mice with macrophage-loaded doxorubicine (DOX) and found that macrophages entered the tumor tissue and effectively delivered the drug directly to cancer cells through a tunneling nanotube pathway. Moreover, it was found that the chemokine receptors CCR2 and CCR4 of drug-loaded macrophages were highly expressed, which enhanced the tropism of macrophages. Hence, it is logical to assume that USIO NPs could be loaded onto Au NFs and carried by cancer tropic macrophagocytes to reach tumors for better cancer MR/CT image formation.

In the present study, our team developed a novel MA-laden nanomedicine platform to realize improved cancer MR/CT imaging. First, citrate-stabilized USIO NPs and Amine-terminated G5 PAMAM dendrimers-stabilized gold nanoparticles (Au DSNPs) were prepared by a solvothermal route mentioned and self-reduction. Then, Au DSNPs and USIO NPs constituted the seed particles via a 1-(3-dimethylaminopropyl)-3-ethylcarbodiimide hydrochloride (EDC)-mediated covalent reactive process and were used to generate Au NFs. After that, we acetylated the amino group at the terminal of PAMAM to change the surface potential of the $\text{Fe}_3\text{O}_4/\text{Au}$ DSNFs. The generated $\text{Fe}_3\text{O}_4/\text{Au}$ DSNFs were loaded in MA for further conveyance to cancers posterior to intravenous injection for MR/CT imaging of tumors (Scheme 1). The generated $\text{Fe}_3\text{O}_4/\text{Au}$ DSNFs were completely characterized by numerous approaches. The cytocompatibility and uptake efficiency via MA were comprehensively assessed. The underlying value of the MA loaded with the $\text{Fe}_3\text{O}_4/\text{Au}$ DSNFs for improved cancer MR/CT imaging was subsequently examined in vivo by mice breast cancer models. For all we know, this is the first research on the development of the MA-laden $\text{Fe}_3\text{O}_4/\text{Au}$ DSNFs platform for enhanced tumor MR/CT image formation.



Scheme 1. Schematic illustration of the preparation of MA@ $\text{Fe}_3\text{O}_4/\text{Au}$ DSNFs for dual-modal imaging of tumors.

2. Materials and Methods

2.1. Synthesis of $\text{Fe}_3\text{O}_4/\text{Au}$ DSNFs

Firstly, the ultrasmall iron oxide was acquired by a solvothermal route introduced in our past research [30]. Meanwhile, G5 PAMAM Au DSNPs were prepared by the self-reduction method [11]. We obtained $\text{Fe}_3\text{O}_4/\text{Au}$ DSNFs through an EDC-mediated covalent reaction with Au DSNPs and EDC-activated USIO NPs based on literature [15]. Briefly, the carboxyl groups of USIO NPs were activated with EDC, then the activated USIO NPs were added dropwise into the solution of Au DSNPs with amino groups on the surface, and finally the $\text{Fe}_3\text{O}_4/\text{Au}$ DSNFs was generated through covalent bonding. The terminal amines of the PAMAM were finally treated with acetyl to reduce the positive surface charge of the hybrid nanomaterials. The generated $\text{Fe}_3\text{O}_4/\text{Au}$ DSNFs have been characterized by different techniques, such as transmission electron microscopy (TEM), dynamic light scatter (DLS), and UV-vis spectra.

2.2. In Vitro Cytotoxicity and Cellular Uptake Assays

Mouse monocyte macrophages (Raw264.7) were incessantly cultivated in the DMEM intermediate. Cytotoxicity of the $\text{Fe}_3\text{O}_4/\text{Au}$ DSNFs relative to Raw264.7 cells was detected using a CCK-8 assay according to the literature [27]. The transwell experiment was carried out to verify whether the tumor-tendency of macrophages changed after incubation with $\text{Fe}_3\text{O}_4/\text{Au}$ DSNFs for 18 h. The cell uptake of the $\text{Fe}_3\text{O}_4/\text{Au}$ DSNFs was evaluated as well

by the ICP-OES method and Prussian blue dyeing. The phenotype of Raw264.7 cells after incubating with Fe₃O₄/Au DSNFs for 6 h were evaluated by flow cytometry (BD FACS Calibur, Franklin Lakes, NJ, USA).

2.3. *In Vivo* MR and CT Imaging of Breast Tumor Model

The mouse breast tumor model was built in male 4–6 weeks old ICR mice for MR and CT imaging. All mice were injected with 2×10^6 4T1 cells into the right legs to form the breast cancer models. Until the cancer dimensions of mice registered 0.45–0.75 cm³, macrophages mediated Fe₃O₄/Au DSNFs ([Fe] = 100 µg, in 0.2 mL PBS) were injected into all mice and similar dosages of free Fe₃O₄/Au DSNFs were injected into the control group for MR image formation. In addition, macrophages mediated Fe₃O₄/Au DSNFs ([Au] = 3 mM, in 0.2 mL PBS) were injected into all mice and a similar dosage of free Fe₃O₄/Au DSNFs were injected into the control group for CT imaging. The *in vivo* breast cancer imaging studies were measured by the CT and MR method. Afterwards, the CT and T₁-weighted MR images of all mice were acquired prior to and posterior to the injection of the MA@Fe₃O₄/Au DSNFs or Fe₃O₄/Au DSNFs at diverse time points.

3. Results and Discussion

3.1. Characterization of Fe₃O₄/Au DSNFs

USIO NPs were first synthesized to be used as seed particles. The results of TEM showed that the diameter of formed USIO NPs is 2.6 ± 0.61 nm (Figure S1a,b). Amine-terminated G5 PAMAM dendrimers-stabilized gold nanoflowers were prepared by a self-reduction method, which displayed a size around 20 nm (Figure 1a). Meanwhile, the particles of Fe₃O₄/Au DSNPs at the size of 15 nm (Figure 1b) were obtained by EDC-activated USIO NPs which reacted with Au DSNPs by an amide linkage. The size of the Fe₃O₄/Au DSNPs measured by TEM is smaller than the individual Au DSNPs, indicating the remarkable interaction between Au DSNPs and USIO NPs, in accordance with the results reported by previous literature [15]. After Fe₃O₄/Au DSNPs merge with an Au growth solution, their sizes gradually grow to 98 nm. It is clear to see the nanoflower structure as shown in Figure 1c.

The zeta potential and hydrodynamic size of USIO NPs, Au DSNPs, Fe₃O₄/Au DSNPs, and Fe₃O₄/Au DSNFs were subsequently tested by DLS. Obviously, the zeta potential of the USIO NPs and Au DSNPs is -24.6 ± 3.1 mV and 23.8 ± 3.5 mV, respectively. The change is supposed to be due to the rich citric acid carboxyl and PAMAM terminal amines on their surface. The surface potentials of the Fe₃O₄/Au DSNPs were measured to be 19.2 ± 2.2 mV, because the hybrid reaction neutralized partial terminal amines of Au DSNPs. In order to shield the residual primary amines of G5 dendrimers, the formed Fe₃O₄/Au DSNPs were acetylated, leading to a reduction of zeta potential to 11.2 ± 2.7 mV. The hydrodynamic size of USIO NPs, Au DSNPs, seed particles, and Fe₃O₄/Au DSNFs is 27.5 ± 2.4 nm, 30.7 ± 7.2 nm, 28.2 ± 3.1 nm, and 265.3 ± 6.9 nm, respectively. Due to the aggregation nature of the nanoparticles in water, an increasing hydrodynamic size was observed in aqueous solutions compared to the data obtained from TEM. However, the hydrodynamic sizes shared a similar variation trend with the TEM results, indicating that the NFs have been successfully prepared.

The structure of Fe₃O₄/Au DSNFs was confirmed by UV-vis (Figure 1d). The results showed that the characteristic ultraviolet absorptions of G5 PAMAM gold particles and Fe₃O₄/Au DSNFs fall at about 520 nm and 820 nm, respectively. It is proven that the Fe₃O₄/Au DSNFs were successfully constructed, which was consistent with the previous literature [15]. In order to assess the steadiness of the Fe₃O₄/Au DSNFs, we surveyed the size and polymer dispersity index (PDI) of Fe₃O₄/Au DSNFs at diverse concentrations within 14 days. As displayed in Figure S2, no apparent changes could be found, suggesting its good colloidal stability and dispersity.

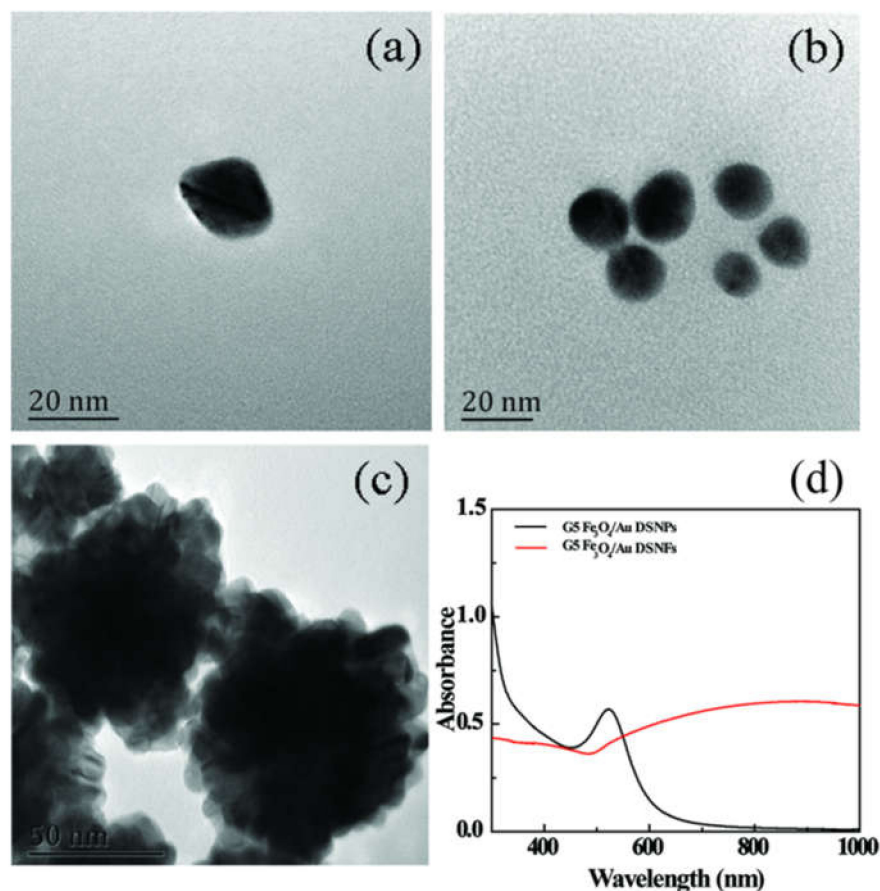


Figure 1. Structural characterization of $\text{Fe}_3\text{O}_4/\text{Au}$ DSNFs. (a) TEM images of Au NPs, (b) TEM images of $\text{Fe}_3\text{O}_4/\text{Au}$ DSNPs, (c) TEM images of $\text{Fe}_3\text{O}_4/\text{Au}$ DSNFs, (d) UV-vis spectrum of $\text{Fe}_3\text{O}_4/\text{Au}$ DSNPs and $\text{Fe}_3\text{O}_4/\text{Au}$ DSNFs.

3.2. *In Vitro* T_1 -Weighted MR Images

As it contains both the radiodense element (Au) and T_1 positive agents (Fe_3O_4), $\text{Fe}_3\text{O}_4/\text{Au}$ DSNFs can be utilized for CT and MR imaging. To verify the MR imaging potential of the USIO NPs and $\text{Fe}_3\text{O}_4/\text{Au}$ DSNFs *in vitro*, their r_1 relaxivity were tested. As shown in Figure 2a, the r_1 relaxivity of the USIO NPs and $\text{Fe}_3\text{O}_4/\text{Au}$ DSNFs were computed to be $0.82 \text{ mM}^{-1} \text{ s}^{-1}$ and $1.22 \text{ mM}^{-1} \text{ s}^{-1}$, separately. It is distinctly shown that the r_1 relaxivity of $\text{Fe}_3\text{O}_4/\text{Au}$ DSNFs is 1.47 times greater than that of the USIO NPs. It is attributed to the fact that USIO NPs were sufficiently dispersed by G5 dendrimer-stabilized Au NPs, while the NFs structure by the seed-mediated approach does not appear to cause remarkable clustering of USIO NPs. Meanwhile, it is clear that USIO NPs and $\text{Fe}_3\text{O}_4/\text{Au}$ DSNFs have shown excellent MR imaging ability, which is strengthened with the rise of Fe concentration. The CT imaging property of $\text{Fe}_3\text{O}_4/\text{Au}$ DSNFs was detected, and a clinical CT contrast agent Loversol was tested as the positive control (Figure 2b). CT images verify that the HU of Loversol and $\text{Fe}_3\text{O}_4/\text{Au}$ DSNFs increase significantly with the increase of concentration Au and I. Moreover, at the same concentration of Au and I, $\text{Fe}_3\text{O}_4/\text{Au}$ DSNFs have a higher attenuation coefficient and a more significant imaging effect. The results demonstrated that the synthesized $\text{Fe}_3\text{O}_4/\text{Au}$ DSNFs can be used as a potential multimodal contrast agent in MR and CT molecular imaging diagnoses.

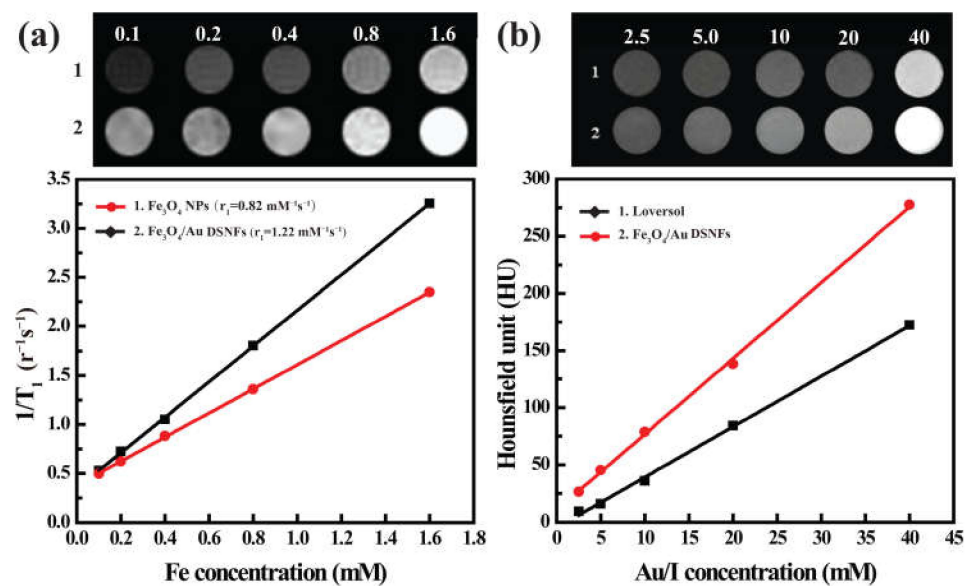


Figure 2. CT and MR imaging properties of the $\text{Fe}_3\text{O}_4/\text{Au}$ DSNFs. (a) T_1 -weighted MR images and linear fitting of $1/T_1$ of the Fe_3O_4 NPs and $\text{Fe}_3\text{O}_4/\text{Au}$ DSNFs at diverse Fe concentrations (1 and 2 refers to USIO NPs and NFs, separately). TE = 12 ms, TR = 377 ms, and ST = 2.0. (b) CT images and CT values (HU) of Loversol and $\text{Fe}_3\text{O}_4/\text{Au}$ DSNFs with diverse concentrations of the radiodense element of Au or I (1 and 2 refers to Omnipaque and NFs, respectively).

3.3. In Vitro Cytotoxicity and Cellular Uptake Assays

The influence of materials on cell vitality is vital for subsequent in vivo imaging applications. Therefore, the cytotoxicity of $\text{Fe}_3\text{O}_4/\text{Au}$ DSNFs was first explored before the in vivo multimode imaging application. The viability of Raw264.7 cells was implemented by CCK-8 assay after a treatment with the $\text{Fe}_3\text{O}_4/\text{Au}$ DSNFs for 24 h (Figure 3a). It is obvious that the cell viability gradually decreased with the rise of Au quantity. However, the viability was still higher than 72% when the Au concentration reached 3 mM, implying that the $\text{Fe}_3\text{O}_4/\text{Au}$ DSNFs register an acceptable cytocompatibility when the Au concentration ranges from 0 mM to 3 mM. To find the cellular uptake efficiency of $\text{Fe}_3\text{O}_4/\text{Au}$ DSNFs by Raw264.7 cells, the Au uptake of Raw264.7 cells co-cultured with the $\text{Fe}_3\text{O}_4/\text{Au}$ DSNFs ($[\text{Au}] = 3 \text{ mM}$) from 2 h to 8 h was assessed in terms of quantity inductively coupled plasma-optical emission spectroscopy (ICP-OES) (Figure 3b). The results show the phagocytic capacity is the highest when Raw264.7 cells were cultivated with $\text{Fe}_3\text{O}_4/\text{Au}$ DSNFs for 6 h. Furthermore, with the increase of Fe concentration, the darker dyeing could be found after the cells were treated with the $\text{Fe}_3\text{O}_4/\text{Au}$ DSNFs based on Fe uptake qualitatively surveyed by Prussian blue staining (Figure S3). The results confirmed that the $\text{Fe}_3\text{O}_4/\text{Au}$ DSNFs can be easily taken up by Raw264.7 cells, which was useful to enhance the multimode imaging ability of the $\text{Fe}_3\text{O}_4/\text{Au}$ DSNFs.

Tumor tropism is a typical peculiarity of macrophages because it can be guided by chemokines and cytokines to the inflammation site. The transwell migration experiment was designed to verify whether the functional properties of macrophages have changed after Raw264.7 cells were incubated with the $\text{Fe}_3\text{O}_4/\text{Au}$ DSNFs for 18 h (Figure 4a). In this experiment, 4T1 cells were utilized. It can be seen that the presence of 4T1 cells has a significant effect on the migration rate of Raw264.7 cells, which is about three times than that in the absence of 4T1 cells. Although the cell migration rate was slightly reduced after co-incubation with $\text{Fe}_3\text{O}_4/\text{Au}$ DSNFs compared with free MAs, the tumor tropism of $\text{MA}@\text{Fe}_3\text{O}_4/\text{Au}$ DSNFs was still significant. It indicates that the activities and roles of Raw264.7 cells are not influenced posterior to the uptake of the $\text{Fe}_3\text{O}_4/\text{Au}$ DSNFs.

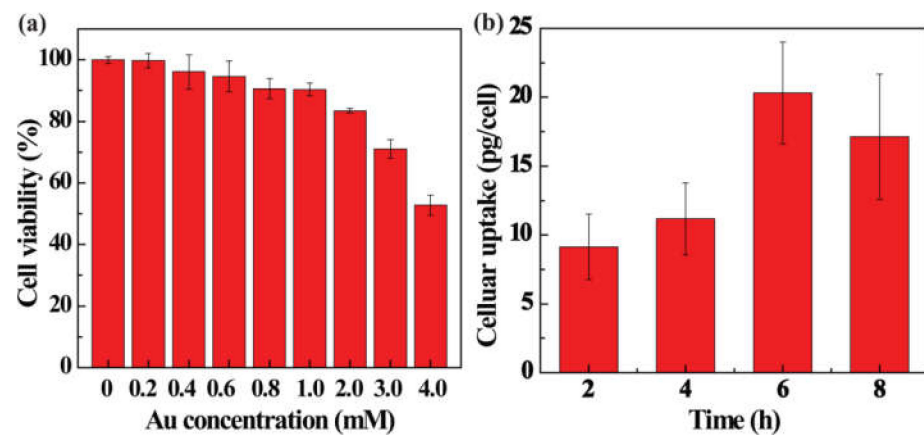


Figure 3. (a) Cell viability of $\text{Fe}_3\text{O}_4/\text{Au}$ DSNFs cultured with Raw264.7 cells in different Fe concentration. (b) Cellular uptake of $\text{Fe}_3\text{O}_4/\text{Au}$ DSNFs with MAs for 2, 4, 6, and 8 h.

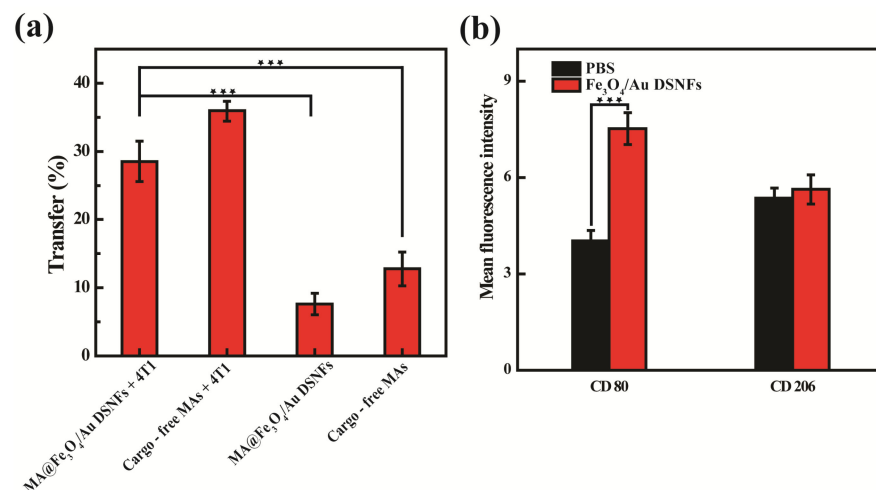


Figure 4. (a) Cell migration rates of Raw264.7 cells to 4T1 cells treated with MA@ $\text{Fe}_3\text{O}_4/\text{Au}$ DSNFs with 4T1 cell-guided, MA with 4T1 cell-guided, MA@ $\text{Fe}_3\text{O}_4/\text{Au}$ DSNFs without 4T1 cell-guided, and MA without 4T1 cell-guided for 18 h. (b) Quantification of CD80 and CD206 expression via flow cytometry for Raw264.7 cells incubating with and without $\text{Fe}_3\text{O}_4/\text{Au}$ DSNFs in the in vitro experiment.

In addition, we must consider that macrophages are easy to differentiate into various phenotypes that exacerbate or resolve the disease. Previous studies have confirmed that iron can activate the differentiation of macrophages to the M1 phenotype [32]. Therefore, it is necessary to detect the activation states and the biomarkers of macrophage phenotypes after the incubation of $\text{Fe}_3\text{O}_4/\text{Au}$ DSNFs. As we know, M1 macrophages could be identified by certain special surface antigens such as CD80 and CD86, while CD206 antigens are expressed in M2 macrophages. Thus, Raw264.7 cells incubated with $\text{Fe}_3\text{O}_4/\text{Au}$ DSNFs for 6 h were analyzed by specific M2 and M1 macrophages antigens CD206 (Figure S4a) and CD80 (Figure S4b) by flow cytometry. For quantitative results, the expression of CD206 by Raw264.7 cells with and without $\text{Fe}_3\text{O}_4/\text{Au}$ DSNFs are 5.36 ± 0.31 and 5.63 ± 0.45 , respectively (Figure 4b). The similar results indicated that the loading of $\text{Fe}_3\text{O}_4/\text{Au}$ DSNFs did not stimulate macrophages to the M2 phenotype. After incubation with and without $\text{Fe}_3\text{O}_4/\text{Au}$ DSNFs the expression level of CD80 are 7.52 ± 0.5 and 4.03 ± 0.32 , respectively (Figure 4b), proving that $\text{Fe}_3\text{O}_4/\text{Au}$ DSNFs activate macrophages to the M1 phenotype. It suggests that the performance of macrophages differentiate toward the M1 phenotype after uptake of the $\text{Fe}_3\text{O}_4/\text{Au}$ DSNFs, possibly exhibiting tumoricidal activity. Thus, the above

results also show that the MA@Fe₃O₄/Au DSNFs have potential applications in cancer therapy.

3.4. In Vivo MR and CT Imaging of Breast Tumor Model

Next, we investigated the capability of Fe₃O₄/Au DSNFs for in vivo duo-modal MR/CT imaging of a subcutaneous tumor model (Figure 5). Free Fe₃O₄/Au DSNFs without Raw264.7 cells mediated were taken as the control group. It can be seen that the tumor regions are progressively illuminated over time posterior to injection of Fe₃O₄/Au DSNFs and MA@Fe₃O₄/Au DSNFs (Figure 5a). Moreover, we obtained the best MR imaging performance at 30 min after injection, which may be attributed to the largest cumulation of MA@Fe₃O₄/Au DSNFs in the tumor region. For contrast, merely a little rise of the MR signal intensity could be detected in Fe₃O₄/Au DSNFs samples. Most importantly, even during metabolism, we noted that MA@Fe₃O₄/Au DSNF could still provide premium imaging of the tumor area after 60 min posterior to injection. It is supposed that macrophages can target to the tumor region, resulting in the better accumulation of MA@Fe₃O₄/Au DSNFs than free Fe₃O₄/Au DSNFs. Besides, the released Fe₃O₄/Au DSNFs via exocytosis could be incessantly utilized for MR imaging of tumors until they are metabolized out of the body, thereby displaying a greater retention time than free Fe₃O₄/Au DSNFs. The quantity outcomes of MR SNR data were evaluated at diverse time points as well (Figure 5b). Within 15–45 min posterior to tail vein injection, the cancer SNR value of MA@Fe₃O₄/Au DSNFs is around 1.5–1.9 times greater than that treated with Fe₃O₄/Au DSNFs ($p < 0.001$). Those results display that the MA@Fe₃O₄/Au DSNFs demonstrate a synergistically improved T₁ imaging effect in contrast to Fe₃O₄/Au DSNFs.

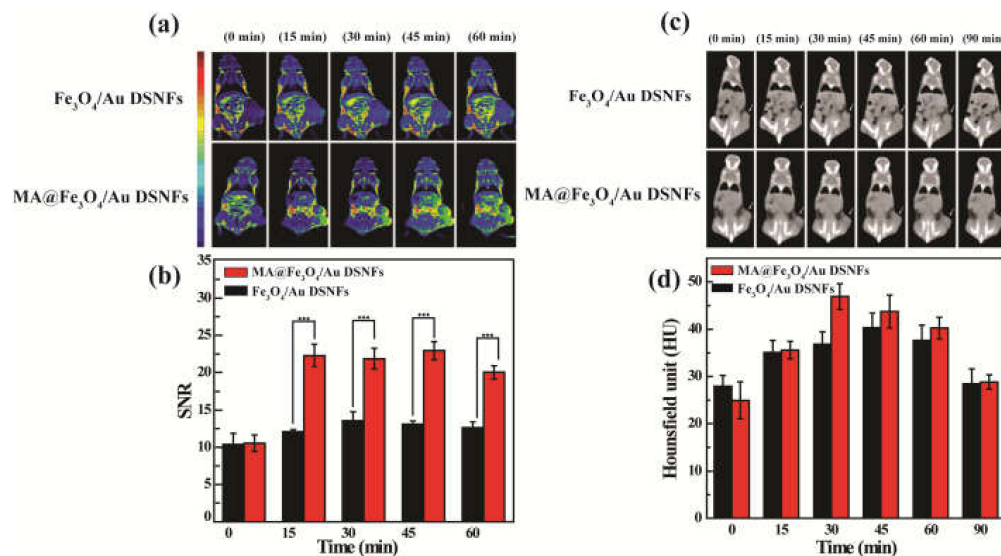


Figure 5. In vivo tumor MR and CT imaging. (a) In vivo T₁-weighted MR images and (b) the corresponding MR SNR of the 4T1 tumor anterior to injection and at diverse time points post-injection of Fe₃O₄/Au DSNFs and MA@Fe₃O₄/Au DSNFs ([Fe] = 100 µg, in 0.2 mL PBS for every mouse), separately (mean ± S.D., $n = 3$). The MR signal intensity of blank (air) was utilized as the background (noise). TE = 12 ms, TR = 377 ms, and ST = 2.0. (c) CT images and (d) corresponding CT values of the 4T1 cancer in ICR mice before and at diverse time points post intravenous injection of the Fe₃O₄/Au DSNFs and MA@Fe₃O₄/Au DSNFs ([Au] = 0.04 M, in 200 µL PBS for every mouse).

Likewise, due to the outstanding effect of Au on CT imaging, we subsequently studied the performance of MA@Fe₃O₄/Au DSNFs for in vivo CT imaging (Figure 5c). As we could see, macrophages facilitated targeted delivery of Fe₃O₄/Au DSNFs to the tumor region, thereby improving the effect of CT imaging compared with free Fe₃O₄/Au DSNFs. The highest resolution CT imaging of a tumor area of MA@Fe₃O₄/Au DSNFs was obtained

after 30 min from tail vein injection. Quantitatively, the CT value of tumor site reached the summit value at 30 min posterior to intravenous injection of MA@Fe₃O₄/Au DSNFs which registered lesser time consumption in comparison with free Fe₃O₄/Au DSNFs, and the summit value (46 HU) is 1.2 times greater than that of free Fe₃O₄/Au DSNFs (39 HU). The entire outcomes validate that a macrophages-laden Fe₃O₄/Au DSNFs delivery nano-system could enhance the accumulation and prolong the retention time of the Fe₃O₄/Au DSNFs in a tumor region. Accordingly, it could be applied for enhanced MR/CT imaging of tumors.

4. Conclusions

In summary, we developed a novel targeted diagnostic platform based on the MA-laden delivery of Fe₃O₄/Au DSNFs for enhanced multimodal imaging of tumors. The prepared Fe₃O₄/Au DSNFs register a size of 98 nm resembling our past research, and are proven to be uniform, colloidally stable, and cytocompatible. It displayed predominant performance on CT and MR imaging with relatively high r_1 relaxivity ($1.22 \text{ mM}^{-1} \text{ s}^{-1}$), and could be well taken up by macrophages with little influence on cell viability so that MA@Fe₃O₄/Au DSNFs could be successfully utilized in the in vivo CT and MR molecular imaging of the breast cancer model. The entire outcome concluded that MA-mediated Fe₃O₄/Au DSNFs are possible to be used as an unusual multimodal contrast agent for tumor diagnosis. Further studies on the PA performance and photothermal treatment effect of the developed MA-laden Fe₃O₄/Au DSNFs should be conducted to build multifunctional nanoplatfoms for precise tumor treatment.

Supplementary Materials: The following are available online at <https://www.mdpi.com/article/10.3390/pharmaceutics13070995/s1>, Figure S1: (a) TEM image and (b) the mean dimension distribution column diagram of USIO NPs; Figure S2: Digital photos of Fe₃O₄/Au DSNFs with diverse molecular rates of Fe/Au (from 1:1 to 6:1), (a) 3 d (b) 5 d (c) 7 d; Figure S3: MA@Fe₃O₄/Au DSNFs with different Fe concentrations (0, 0.44, 0.88, and 1.76 mM) to incubate with Raw264.7 cells for 6 h and stain with Prussian blue reagent; Figure S4: Identification of special CD markers in Raw264.7 cells via flow cytometric method. Raw264.7 cells were dyed with fluorescence conjugated antibodies fluorescein phycoerythrin conjugated rat anti mouse (a) CD206 and (b) CD80.

Author Contributions: Conceptualization, Y.P., X.W., Y.W., Y.G., R.G., X.S., and X.C.; writing—original draft preparation, Y.P., X.W., and X.C.; writing—review and editing, Y.P., X.W., Y.W., Y.G., R.G., X.S., and X.C.; supervision, X.S. and X.C.; project administration, R.G., X.S., and X.C. All authors have read and agreed to the published version of the manuscript.

Funding: This study was financially supported by Shanghai Pujiang Program(19PJD001), the Science and Technology Commission of Shanghai Municipality (20DZ2254900 and 19XD1400100), National Natural Science Foundation of China (21773026, 21875031 and 81761148028), the National Key R&D Program (2017YFE0196200).

Institutional Review Board Statement: All animal procedures were performed in accordance with the Guidelines for Care and Use of Laboratory Animals of Songjiang Central Hospital and approved by the Animal Ethics Committee of the Institutional Animal Care and Use Committees (IACUC), and also in compliance with the policy of the National Ministry of Health.

Informed Consent Statement: Not applicable.

Data Availability Statement: Not applicable.

Acknowledgments: Not applicable.

Conflicts of Interest: The authors declare no conflict of interest. The funders had no role in the design of the study; in the collection, analyses, or interpretation of data; in the writing of the manuscript, or in the decision to publish the results.

References

1. Liu, Y.; Bhattarai, P.; Dai, Z.; Chen, X. Photothermal therapy and photoacoustic imaging via nanotheranostics in fighting cancer. *Chem. Soc. Rev.* **2019**, *48*, 2053–2108. [[CrossRef](#)]
2. Yang, Y.; Yang, H.; Tao, L.; Yao, J.; Wang, W.; Zhang, K.; Luquot, L. Microscopic Determination of Remaining Oil Distribution in Sandstones with Different Permeability Scales Using Computed Tomography Scanning. *J. Energy Resour. Technol.* **2019**, *141*, 1–17. [[CrossRef](#)]
3. Yu, F.; Li, J.; Yang, Y.; Cheng, Y.; Ni, X.; Wei, K.; Liu, Z. RGD-Tagged Microbubbles Generated by Versatile Fabrication Protocols for In Vitro Cell Targeting and In Vivo Mouse Imaging of Tumor Vascularization. *Sci. Adv. Mater.* **2020**, *12*, 725–732. [[CrossRef](#)]
4. Chen, Y.-S.; Zhao, Y.; Yoon, S.J.; Gambhir, S.S.; Emelianov, S. Miniature gold nanorods for photoacoustic molecular imaging in the second near-infrared optical window. *Nat. Nanotechnol.* **2019**, *14*, 465–472. [[CrossRef](#)]
5. Sonn, G.A.; Fan, R.E.; Ghanouni, P.; Wang, N.; Brooks, J.D.; Loening, A.; Daniel, B.L.; To'O, K.J.; Thong, A.E.; Leppert, J.T. Prostate Magnetic Resonance Imaging Interpretation Varies Substantially Across Radiologists. *Eur. Urol. Focus* **2019**, *5*, 592–599. [[CrossRef](#)]
6. Laurent, S.; Forge, D.; Port, M.; Roch, A.; Robic, C.; Elst, L.V.; Muller, R.N. Magnetic Iron Oxide Nanoparticles: Synthesis, Stabilization, Vectorization, Physicochemical Characterizations, and Biological Applications. *Chem. Rev.* **2010**, *110*, 2574. [[CrossRef](#)]
7. Dykman, L.A.; Khlebtsov, N.G. Gold Nanoparticles in Biology and Medicine: Recent Advances and Prospects. *Acta Nat.* **2011**, *3*, 34–55. [[CrossRef](#)]
8. Cui, Y.-R.; Hong, C.; Zhou, Y.-L.; Li, Y.; Gao, X.-M.; Zhang, X.-X. Synthesis of orientedly bioconjugated core/shell Fe₃O₄@Au magnetic nanoparticles for cell separation. *Talanta* **2011**, *85*, 1246–1252. [[CrossRef](#)] [[PubMed](#)]
9. Li, J.; Shi, X.; Shen, M. Hydrothermal Synthesis and Functionalization of Iron Oxide Nanoparticles for MR Imaging Applications. *Part. Part. Syst. Charact.* **2014**, *31*, 1223–1237. [[CrossRef](#)]
10. Joumaa, N.; Toussay, P.; Lansalot, M.; Elaissari, A. Surface modification of iron oxide nanoparticles by a phosphate-based macromonomer and further encapsulation into submicrometer polystyrene particles by miniemulsion polymerization. *J. Polym. Sci. Part A Polym. Chem.* **2007**, *46*, 327–340. [[CrossRef](#)]
11. Li, J.; Hu, Y.; Yang, J.; Wei, P.; Sun, W.; Shen, M.; Zhang, G.; Shi, X. Hyaluronic acid-modified Fe₃O₄@Au core/shell nanostars for multimodal imaging and photothermal therapy of tumors. *Biomaterials* **2015**, *38*, 10–21. [[CrossRef](#)]
12. Elahi, N.; Kamali, M.; Baghersad, M.H. Recent biomedical applications of gold nanoparticles: A review. *Talanta* **2018**, *184*, 537–556. [[CrossRef](#)] [[PubMed](#)]
13. Huang, K.-J.; Liu, Y.-J.; Liu, Y.-M.; Wang, L.-L. Molybdenum disulfide nanoflower-chitosan-Au nanoparticles composites based electrochemical sensing platform for bisphenol A determination. *J. Hazard. Mater.* **2014**, *276*, 207–215. [[CrossRef](#)] [[PubMed](#)]
14. Saucedo, H.E.; Salazar, F.; Pérez, L.A.; Garzón, I.L. Size and Shape Dependence of the Vibrational Spectrum and Low-Temperature Specific Heat of Au Nanoparticles. *J. Phys. Chem. C* **2013**, *117*, 25160–25168. [[CrossRef](#)]
15. Lu, S.; Li, X.; Zhang, J.; Peng, C.; Shen, M.; Shi, X. Dendrimer-Stabilized Gold Nanoflowers Embedded with Ultrasmall Iron Oxide Nanoparticles for Multimode Imaging-Guided Combination Therapy of Tumors. *Adv. Sci.* **2018**, *5*, 1801612. [[CrossRef](#)]
16. Clark, A.J.; Davis, M.E. Increased brain uptake of targeted nanoparticles by adding an acid-cleavable linkage between transferrin and the nanoparticle core. *Proc. Natl. Acad. Sci. USA* **2015**, *112*, 12486–12491. [[CrossRef](#)]
17. Wang, Y.; Xie, Y.; Li, J.; Peng, Z.-H.; Sheinin, Y.; Zhou, J.; Oupický, D. Tumor-Penetrating Nanoparticles for Enhanced Anticancer Activity of Combined Photodynamic and Hypoxia-Activated Therapy. *ACS Nano* **2017**, *11*, 2227–2238. [[CrossRef](#)]
18. Lu, W.; Singh, A.K.; Khan, S.A.; Senapati, D.; Yu, H.; Ray, P.C. Gold Nano-Popcorn-Based Targeted Diagnosis, Nanotherapy Treatment, and In Situ Monitoring of Photothermal Therapy Response of Prostate Cancer Cells Using Surface-Enhanced Raman Spectroscopy. *J. Am. Chem. Soc.* **2010**, *132*, 18103–18114. [[CrossRef](#)]
19. Tamarov, K.; Sviridov, A.; Xu, W.; Malo, M.; Andreev, V.; Timoshenko, V.; Lehto, V.-P. Nano Air Seeds Trapped in Mesoporous Janus Nanoparticles Facilitate Cavitation and Enhance Ultrasound Imaging. *ACS Appl. Mater. Interfaces* **2017**, *9*, 35234–35243. [[CrossRef](#)]
20. Cheng, L.; Yang, K.; Li, Y.; Chen, J.; Wang, C.; Shao, M.; Lee, S.-T.; Liu, Z. Facile Preparation of Multifunctional Upconversion Nanoprobes for Multimodal Imaging and Dual-Targeted Photothermal Therapy. *Angew. Chem. Int. Ed.* **2011**, *50*, 7385–7390. [[CrossRef](#)] [[PubMed](#)]
21. Zhu, W.; Zhao, L.; Fan, Y.; Zhao, J.; Shi, X.; Shen, M. 131 I-Labeled Multifunctional Polyphosphazene Nanospheres for SPECT Imaging-Guided Radiotherapy of Tumors. *Adv. Heal. Mater.* **2019**, *8*, e1901299. [[CrossRef](#)] [[PubMed](#)]
22. Tang, Y.; Wang, X.; Li, J.; Nie, Y.; Liao, G.; Yu, Y.; Li, C. Overcoming the Reticuloendothelial System Barrier to Drug Delivery with a “Don't-Eat-Us” Strategy. *ACS Nano* **2019**, *13*, 13015–13026. [[CrossRef](#)]
23. Batrakova, E.; Kabanov, A. Cell-mediated drug delivery to the brain. *J. Drug Deliv. Sci. Technol.* **2013**, *23*, 419–433. [[CrossRef](#)]
24. Krantz, A. Red Cell-Mediated Therapy: Opportunities and Challenges. *Blood Cells Mol. Dis.* **1997**, *23*, 58–68. [[CrossRef](#)]
25. Roger, M.; Clavreul, A.; Venier-Julienne, M.-C.; Passirani, C.; Sindji, L.; Schiller, P.; Montero-Menei, C.; Menei, P. Mesenchymal stem cells as cellular vehicles for delivery of nanoparticles to brain tumors. *Biomaterials* **2010**, *31*, 8393–8401. [[CrossRef](#)]
26. Aboody, K.S.; Brown, A.; Rainov, N.G.; Bower, K.A.; Liu, S.; Yang, W.; Small, J.E.; Herrlinger, U.; Ourednik, V.; Black, P.M.; et al. Neural stem cells display extensive tropism for pathology in adult brain: Evidence from intracranial gliomas. *Proc. Natl. Acad. Sci. USA* **2000**, *97*, 12846–12851. [[CrossRef](#)] [[PubMed](#)]

27. An, L.; Wang, Y.; Lin, J.; Tian, Q.; Xie, Y.; Hu, J.; Yang, S.-P. Macrophages-Mediated Delivery of Small Gold Nanorods for Tumor Hypoxia Photoacoustic Imaging and Enhanced Photothermal Therapy. *ACS Appl. Mater. Interfaces* **2019**, *11*, 15251–15261. [[CrossRef](#)]
28. Batrakova, E.V.; Gendelman, H.E.; Kabanov, A. Cell-mediated drug delivery. *Expert Opin. Drug Deliv.* **2011**, *8*, 415–433. [[CrossRef](#)]
29. Kim, J.W.; Auffinger, B.; Spencer, D.A.; Miska, J.; Chang, A.L.; Kane, J.R.; Young, J.S.; Kanojia, D.; Qiao, J.; Mann, J.F.; et al. Single dose GLP toxicity and biodistribution study of a conditionally replicative adenovirus vector, CRAd-S-pk7, administered by intracerebral injection to Syrian hamsters. *J. Transl. Med.* **2016**, *14*, 134. [[CrossRef](#)]
30. Hao, X.; Xu, B.; Chen, H.; Wang, X.; Zhang, J.; Guo, R.; Shi, X.; Cao, X. Stem cell-mediated delivery of nanogels loaded with ultrasmall iron oxide nanoparticles for enhanced tumor MR imaging. *Nanoscale* **2019**, *11*, 4904–4910. [[CrossRef](#)] [[PubMed](#)]
31. Guo, L.; Zhang, Y.; Yang, Z.; Peng, H.; Wei, R.; Wang, C.; Feng, M. Tunneling Nanotubular Expressways for Ultrafast and Accurate M1 Macrophage Delivery of Anticancer Drugs to Metastatic Ovarian Carcinoma. *ACS Nano* **2019**, *13*, 1078–1096. [[CrossRef](#)] [[PubMed](#)]
32. Handa, P.; Thomas, S.; Morgan-Stevenson, V.; Maliken, B.D.; Gochanour, E.; Boukhar, S.; Yeh, M.M.; Kowdley, K.V. Iron alters macrophage polarization status and leads to steatohepatitis and fibrogenesis. *J. Leukoc. Biol.* **2019**, *105*, 1015–1026. [[CrossRef](#)] [[PubMed](#)]